The Astrophysical Journal, 987:131 (13pp), 2025 July 10 https://doi.org/10.3847/1538-4357/add3f8

Intergalactic Absorption Confounding Circumgalactic Observations

Itai Bromberg[1], Kartick C. Sarkar[2,3,4], Haggar Ashkenazy[1], Orly Gnat[1], and Yuval Birnboim[1]
[1] Center for Astrophysics and Planetary Science, Racah Institute of Physics, The Hebrew University, Jerusalem 91904, Israel; itai.bromberg@mail.huji.ac.il
[2] Department of Astrophysics, Tel Aviv University, Tel Aviv 69978, Israel
[3] Department of Space, Planetary & Astronomical Sciences and Engineering, Indian Institute of Technology Kanpur, Kanpur, India
[4] Raman Research Institute, Bengaluru, 560 080, India
Received 2024 July 25; revised 2025 April 14; accepted 2025 May 1; published 2025 July 3

Abstract

The origin of warm ions in the circumgalactic medium (CGM) surrounding massive galaxies remains a mystery. In this paper, we argue that a significant fraction of the observed warm-ion columns may arise in the intergalactic medium (IGM) surrounding galactic halos. We use a simple spherical collapse model of the dark matter halos and their baryonic content to compute the evolving ion fractions within and outside virial halos. We show that the photoionized IGM may produce a thick blanket of warm ions around the CGM, with column densities comparable to observed values near galaxies, which may therefore contaminate CGM observations. We compare our results with observations, and find that our models qualitatively reproduce the overall O VI columns as well as their trend with the impact parameter and halo mass. We find that the IGM contribution to the observed column depends on galaxy mass and impact parameter, and becomes comparable to the total observed values in galaxies with virial masses exceeding a few times $10^{11}\,M_{\odot}$, as well as across much of the observed area ($b \gtrsim 0.5R_{\rm vir}$) of lower-mass halos. We therefore suggest that theoretical interpretations of CGM-survey observations must consider the possible contribution of the surrounding IGM. We note that more sophisticated (3D) models are required to consider the possibility of nonunity covering fractions suggested by the data. Although our simplified model suggests that it may be possible to kinematically distinguish between CGM and IGM origins through the absorption-line profiles, this distinction is likely unfeasible.

Unified Astronomy Thesaurus concepts: Galaxies (573); Galaxy dark matter halos (1880); Intergalactic medium (813); Circumgalactic medium (1879); Hubble Space Telescope (761); Quasar absorption line spectroscopy (1317); Warm-hot intergalactic medium (1786); Ultraviolet surveys (1742)

1. Introduction

The circumgalactic medium (CGM) plays an essential role in galaxy formation and evolution, by controlling gas inflow into galaxies and outflow from them. While various aspects of the complex, multiphase CGM have been extensively studied, the roles that different physical processes play in determining its internal structure and ionization properties remain unclear and are the focus of intense observational and theoretical work (J. X. Prochaska et al. 2011b; J. Tumlinson et al. 2011, 2017; S. Muzahid et al. 2012; S. Shen et al. 2012; J. K. Werk et al. 2013, 2016; N. Lehner et al. 2014; B. D. Oppenheimer et al. 2016; J. Stern et al. 2016; Y. Faerman et al. 2017, 2020; T. A. Gutcke et al. 2017; J. Suresh et al. 2017). The cosmological theory of galaxy formation indicates that galactic halos form as gas from the diffuse intergalactic medium (IGM) falls onto the dense regions where galaxies form. While dark matter (DM) particles oscillate about the center of the potential well, baryons are shock-heated to a "virial temperature," corresponding to the mass of the forming galaxy. These shock-heated halos are natural sites for the production of highly ionized species. However, warm ions may also be produced outside the shocked halo in the surrounding IGM. In this region, the baryonic density and temperature profiles are still affected by the halo's gravity, as well as by radiation fields (shock self-radiation, UV background, etc.), strong outflows, cosmic rays, and the inhomogeneity of the cosmic web.

Observational campaigns such as the COS-Halos survey (J. Tumlinson et al. 2011), IMACS survey (S. D. Johnson et al. 2015), or CGM^2 survey (K. Tchernyshyov et al. 2022) have examined the extent of warm ions (e.g., C IV, O VI) surrounding galaxies, as revealed via absorption features in the spectra of background quasars. These studies focus on $\gtrsim L_{\star}$ galaxies ($10^{11.5} \lesssim M_{\rm halo} \lesssim 10^{13}\,M_{\odot}$) at various impact parameters ($10 \lesssim b \lesssim 400$ kpc) and relatively low redshifts ($0.1 \lesssim z \lesssim 0.6$). The COS-Halos survey (J. Tumlinson et al. 2011) demonstrates the existence of O VI absorption at impact parameters up to 150 kpc, with no apparent trend of the column density with impact parameter within this range. Later, S. D. Johnson et al. (2015) used a larger data sample (COS-Halos+IMACS), and showed that no O VI absorption is detected at impact parameters above the virial radius, with upper limits $\sim 10^{13.4}$ cm^{-2}. Their findings suggest that O VI resides primarily within the halo.[5] K. Tchernyshyov et al. (2022) used the CGM^2 data sample to study the extent of O VI absorption. They found that O VI is detected out to their maximal surveyed impact parameter of $\sim$400 kpc, without any particular trend, and with upper limits of order 10^{14} cm^{-2}. According to their fit, significant O VI columns may persist up to (2–3)R_{200}, depending on the halo mass. For lower-mass ($\gtrsim 0.1L_{\star}$) galaxies, J. X. Prochaska et al. (2011b) used the LCO/WFCCD survey (J. X. Prochaska et al. 2011a) to explore a much larger range of impact parameters extending out to $\sim$1000 kpc. They found a large covering fraction of O VI

[5] However, they state that the upper limits of $N_{\rm OVI} > 10^{14}$ cm^{-2} are not shown, as they do not provide significant constraints. See S. D. Johnson et al. (2015) for details.

outside the galactic halos, particularly for sub-$L_\star$ galaxies. They associated it with the diffuse medium surrounding individual galaxies. The prevalence of O VI in and around galactic halos thus remains inconclusive.

Detailed 3D cosmological simulations of galaxy formation attempt to reproduce key trends in observational surveys by invoking various physical processes and assumptions (e.g., radiative cooling, ionization, star formation and evolution, chemical enrichment, wind feedback, black hole growth, AGN feedback, cosmic dust, etc.). D. Nelson et al. (2018) used the IllustrisTNG simulations to estimate the O VI abundance around galaxies. They found that O VI columns persist out to an impact parameter of 10 Mpc, due to contributions by nearby satellite halos and the IGM (Figure 9 therein). They showed that, although the halo's contribution to the O VI column density drops at roughly the virial radius, there are significant contributions from other sources outside the central halo that prevent a distinct cutoff in the column density.

B. D. Oppenheimer et al. (2018) used EAGLE zoom-in simulations to probe O VI columns at impact parameters below ~300 kpc. Their results indicate a slow decline in the O VI column with impact parameter, regardless of halo mass (see Figure 2 therein). In a later paper by S. H. Ho et al. (2021), an EAGLE simulation also produced a flat O VI column density versus impact parameter profile, with contributions from gas outside $3R_{\rm vir}$. S. Appleby et al. (2023) used SIMBA to study different ion absorption features and their origin. They estimated that O VI absorption comprises roughly equal contributions from the gas inside and outside the halo (their Figure 7 and analysis therein).

An alternative to cosmological hydrodynamic simulations is the use of semi-analytic 1D models, which aim to explain the observed trends by focusing on key physical processes. Several works have focused on identifying the origin of O VI and the ionization mechanisms which dominated its production. J. Stern et al. (2018) considered the possibility that O VI is produced either in the shocked halo or in a low-pressure photoionized layer outside the accretion shock. Their low-pressure scenario requires that the accretion shock be located well within $R_{\rm vir}$. This low-pressure O VI phase is disfavored by cosmological simulations but can reproduce the observed properties of O VI as well as other absorption features.

M. McQuinn & J. K. Werk (2018) and Z. Qu & J. N. Bregman (2018a) explored the dominant ionization mechanism for O VI production in the CGM. M. McQuinn & J. K. Werk (2018) included radiative cooling and feedback, and showed that inside the halo O VI is probably produced collisionally, with large cooling gas flows regulated by feedback. Z. Qu & J. N. Bregman (2018a) considered a similar model but also took into account photoionization and steady-state cooling, and demonstrated that photoionization may play a key role in lower-mass halos, as well as in the outskirts of massive halos due to the lower densities.

G. M. Voit (2019) introduced precipitation-regulated feedback models, which account for the relatively constant O VI column density over large spans of halo masses and impact parameters. The emphasis on precipitation has been inspired by the velocity profiles of detected O VI, which do not exceed the halos' escape velocity. This suggests that the gas is circulated inside the halo. Furthermore, this supports the notion that the CGM is multiphased, consistent with the simultaneous detection of various ionic species.

In Y. Faerman et al. (2017), a 1D multiphase semi-analytic model based on isothermal hydrostatic profiles was presented. Assuming turbulence-driven log-normal distributions for the densities and temperatures of both the warm ($\sim 10^4$ K) and hot phases, the model reproduced the detections and upper limits from J. Tumlinson et al. (2011) and S. D. Johnson et al. (2015). Y. Faerman et al. (2020) extended the multiphase model to isentropic profiles, and allowed for radius-dependent temperatures and nonthermal contributions. Their profiles for the hot gas were calibrated using data from J. Tumlinson et al. (2011) and S. D. Johnson et al. (2015). As these models extend only slightly beyond $R_{\rm vir}$, they predict a decline in column density at larger radii.

While warm-ion column densities serve as common diagnostics for CGM analysis and interpretation, theoretical models do not usually account for the warm ions produced outside the shock radius, where the halo's presence still affects the baryon density profile. Computationally, even though simulation-based studies may naturally include this component, they do not focus on the role that the IGM plays in absorption-line observations. This is particularly true for low-mass galaxies ($M_{\rm vir} \lesssim 10^{11}\ M_\odot$), where observations show a significant presence of O VI in contrast to many theoretical CGM models that fail to predict such behavior (see Figure 6 in K. Tchernyshyov et al. 2022; but also see Z. Qu & J. N. Bregman 2018a). This further motivates us to study the IGM contribution to the warm ions at different mass scales. As we will see, in our model the origin of O VI around low-mass galaxies is mainly from the surrounding IGM and not the CGM.

In this work, we argue that the gravitational focusing around halos, which is a natural and unavoidable consequence of structure formation in Lambda cold dark matter (ΛCDM) cosmology, creates a favorable site for warm-ion production (including O VI) via photoionization by the ambient background radiation. We demonstrate this notion using a highly simplified 1D toy model. We show that significant amounts of O VI should naturally arise outside $R_{\rm shock}$, thus increasing—and sometimes dominating—the observed columns of O VI and other key ions around galaxies.

In Section 2, we describe our simplified 1D model. This includes the evolving properties of the DM halos and the distribution and ionization properties of the baryonic matter both within and outside galactic halos. In Section 3, we discuss the observational signatures that arise in our simplified halos. We compute the expected absorption-line columns and discuss the relative contributions of the shocked gas within the halo versus photoionized gas in the IGM to the total absorption-line signatures. We discuss the possibility of discerning them observationally based on their kinematic properties. In Section 4, we conclude by directly comparing our model's IGM columns with observations, demonstrating that the IGM may give rise to O VI columns comparable to observed values. We summarize in Section 5.

2. Model Description

We use a simple 1D cosmological toy model to study the impact of the halos' gravitational potentials and the UV background on the warm-ion production in halos and their surrounding IGM. The model consists of three major components: (i) a redshift-dependent DM density profile, (ii) evolving baryonic density and velocity profiles, and (iii) the corresponding temperature and ionization states of the baryonic matter. We describe these model constituents below.

2.1. Spherical Collapse Model

A simplified model for the DM halo profiles is constructed by tracing the evolution of initial overdensity perturbations solely under the influence of gravity in an Einstein–de Sitter (EdS) cosmology. The analytical solutions in EdS cosmology neglect the impact of Λ on the time evolution and growth rate of the halos. However, this omission is not expected to significantly affect the structure within the turnaround radius, where gravitational forces dominate the Λ-driven expansion. We follow the numerical procedures used in Y. Birnboim & A. Dekel (2003) to set the initial conditions for each 1D spherical simulation. Our profiles are constructed from shells, each tracing a cycloid of the form

$$r = A(1 - \cos\eta), \tag{1}$$

$$t = B(\eta - \sin\eta) \tag{2}$$

(e.g., B. Ryden 2016), where η is the conformal time.

We determine each shell's free parameters (A and B) by imposing two requirements: one at an early linear stage, and the other at the epoch of virialization. First, we require that the mass enclosed within r at some early linear stage ($\eta \ll 1$), satisfies that the overdensity at that time, $\delta(M) \equiv \bar{\rho}/\rho_u - 1$, is proportional to the ΛCDM correlation function of the power spectrum of the universe (A. Dekel 1981). In this expression, $\bar{\rho}$ is the average density inside r, and ρ_u is the universal density. The proportionality constant between $\delta(M)$ and the correlation function can be determined by requiring that a specific mass virializes at a specific time after the Big Bang within our EdS framework. For each shell, we fix B by requiring that at the time of the shell's perspective virialization (when $\eta = 3\pi/2$), the radius r and the time t will satisfy $r = r_{\rm vir}$ and $t = r_{\rm vir}/v_{\rm vir}$, with $v_{\rm vir}^2 = GM/r_{\rm vir}$ and with M the mass enclosed within that shell. This ensures that the infall velocity at this stage is $v_{\rm vir}$.

Here, we calculate profiles with collapsed masses (at $z = 0$) between 10^{11} and $10^{14}\,M_\odot$. We solve Equations (1) and (2) for 1000 shells with the outermost shells exceeding the virial and turnaround radii. The DM density at a given radius is calculated numerically by differentiating the mass with respect to the radii of two adjacent shells at each time (see Y. Birnboim & A. Dekel 2003 for more details), and the results are then mapped onto a regular r–t grid extending to 10 Mpc.

2.2. Gaseous Halo

Given the evolving DM profiles, we compute the properties of the baryonic matter both within and outside the shock radius, defined as

$$R_{\rm shock} = f_{\rm shock} R_{\rm vir}, \tag{3}$$

where $f_{\rm shock}$ is a dimensionless multiplication factor. We explore different values of $f_{\rm shock}$ (0.5, 1, 1.5, and 2) to account for uncertainties in the extent of the virialized gas. By setting $\eta = 1.5\pi$ in Equation (1), one obtains the virial radius. The virial radii of present-day halos with DM masses of $10^{11}, 10^{12}, 10^{13}$, and $10^{14}\,M_\odot$ are $R_{\rm vir} \approx 100, 215, 465$, and 1000 kpc, respectively.[6]

We set the gas density to be everywhere proportional to the evolving DM density,

$$\rho_{\rm gas}(r) = f_b\,\rho_{\rm dm}(r), \tag{4}$$

with $f_b = 0.165$ the universal baryonic fraction (Planck Collaboration et al. 2016; see $f_b = 0.13$ in Y. Birnboim & A. Dekel 2003).

For the velocities, we follow Y. Birnboim & A. Dekel (2003) and set

$$v = v_{\rm vir}\frac{\sin\eta}{1 - \cos\eta} \tag{5}$$

outside $R_{\rm shock}$. Inside the halo, we set $v_{\rm CGM} = 0$.

2.3. Metallicity

For the baryonic component, we assume a metallicity

$$Z = \begin{cases} 0.03\,Z_\odot, & r \geqslant R_{\rm shock} \\ 0.1\,Z_\odot, & r < R_{\rm shock}, \end{cases}$$

inspired by CGM (e.g., N. Lehner et al. 2019) and IGM ($Z = 0.02$–$0.05\,Z_\odot$; e.g., T. Dalton et al. 2021, 2022) observations.

Determining the metallicity in and around halos is an active area of research (e.g., R. P. C. Wiersma et al. 2011; E. Gatuzz et al. 2024; C. Strawn et al. 2024), with a broad range of possible values. Consequently, the absorption-line column densities may need to be adjusted once a "typical" metallicity is established. In the CGM, the metal-ion columns are generally proportional to the metallicity. The IGM columns are slightly more sensitive to metallicity due to the impact it may have on the thermal properties of the gas (see below). The sensitivity of the results to metallicity is examined in Section 3.3.

2.4. Temperature and Ionization State

When determining the thermal and ionization properties of the gas, we assume that the gas is everywhere (both within and outside the halo) exposed to the F. Haardt & P. Madau (2012) redshift-dependent metagalactic UV background radiation field. Given the radiation field, we use CLOUDY v17.01 (G. J. Ferland et al. 2017; M. Chatzikos et al. 2023) to obtain the thermal equilibrium temperatures and ion fractions as described below.

We assume that the gas within $R_{\rm shock}$ has a uniform metallicity $Z = 0.1\,Z_\odot$, and a temperature $T_{\rm CGM}$ such that

$$T_{\rm CGM} = \max(T_{\rm PIE}, T_{\rm vir}). \tag{6}$$

In this expression, $T_{\rm vir}$ is the virial (collisional shock) temperature, which depends on the halo's mass and the redshift. We follow J. L. Johnson (2012, Equation (1) therein), and set

$$T_{\rm vir} = 4 \times 10^4 \left(\frac{\mu}{1.2}\right)\left(\frac{M_{\rm vir}}{10^8 h^{-1} M_\odot}\right)^{2/3}\left(\frac{1+z}{10}\right)\,{\rm K}, \tag{7}$$

where $h \approx 0.7$ is the dimensionless Hubble constant, and μ is the mean molecular weight ($\approx$0.6 for a fully ionized gas). This $T_{\rm vir}$–$M_{\rm vir}$ relation is based on 3D hydrodynamical simulations. While this temperature is not necessarily self-consistent with

[6] Note that our EdS assumption yields virial radii smaller than those expected in ΛCDM. For example, our 215 kpc EdS radius of the $10^{12}\,M_\odot$ halo is $\sim$20% too small compared to the $\sim$260 kpc ΛCDM value.

the spherical collapse model, it better represents the O VI production potential of the halos.

$T_{\rm PIE}$ is the thermal equilibrium temperature, which, given the redshift-dependent background radiation, is a function of the local density, $\rho_{\rm gas}(r)$.

For the ionization of the CGM gas, we take into account the combined impact of collisional ionization at the (forced) halo temperature $T_{\rm CGM}$ (Equation 6) and photoionization by the ambient background. We refer to this ionization state as the collisional photoionization equilibrium (CPIE).

For the IGM, the ionization and thermal states of the gas are computed assuming thermal and ionization equilibrium in the presence of a metagalactic UV background.

2.5. Column Densities

Given the run of ion fractions with radius, we can now compute the column densities as functions of the impact parameter. The column density of element m with ionization level i is given by

$$N_i^m(b) = \int n_i^m(s)ds = 2\int_b^{r_{\rm max}} \frac{n^m(r)x_i^m(r)}{\sqrt{1-\left(\frac{b}{r}\right)^2}}dr, \quad (8)$$

where we integrate along a line of sight intersecting the halo at an impact parameter b. $n_i^m(s)$ is the number density of element m in ionization state i. In the second integral, x_i^m is the ion fraction of element m at ionization level i, $n^m = n_{\rm H}A^m Z$ is the number density of element m, $n_{\rm H}$ is the total hydrogen number density, A^m is the solar elemental abundance of m, and Z is the metallicity. The factor of 2 is a geometrical factor that accounts for the two sides of the spherical halo.

Since we focus on the ions produced outside the galactic disk, we do not integrate over radii smaller than $0.1R_{\rm vir}$. The interstellar medium within the galactic disk would contaminate any detection at lower impact parameters.

When estimating the IGM contribution to the total absorption-line signatures, we set the maximal integration radius, $r_{\rm max} = 3$ Mpc. In our model, this outer radius corresponds to an expansion velocity offset of up to $\sim$200 km s^{-1} for halos with masses in the range $10^{10.5}$–$10^{13}\,M_\odot$ at $z \simeq 0.2$.

2.6. Absorption-line Kinematics

Given the density, temperature, and velocity distribution in our halos, we compute the kinematic line profiles at a given impact parameter. In doing so, we assume that the line profile within each shell is well approximated by a Gaussian profile at the appropriate temperature, centered about the shells' velocity, and we accumulate the optical depth per frequency through the different shells. The numerical procedure is briefly described in the Appendix.

To validate this kinematic approximation, we also use the Trident Python package (C. B. Hummels et al. 2017). Trident computes absorption-line profiles given the density, temperature, and velocity profiles. This module is set to simulate an observation with the Cosmic Origins Spectrograph (COS) on board the Hubble Space Telescope using a G130M line-spread function kernel. Trident also introduces the Milky Way foreground and a Gaussian noise to the simulated line for a more direct comparison with observations.

We performed these calculations, including all the shells between $\max(0.1R_{\rm vir}, b) - 3$ Mpc for the total observed columns, and again for the IGM—this time including only shells that are outside the halo, between $\max(R_{\rm shock}, b) - 3$ Mpc.

2.7. Limitations

Our constructed CGM model is highly simplified and does not accurately capture all the details of astrophysical halos: It does not account for the morphological, thermal, and dynamical complexities of the multiphase CGM or the radiative and dynamical properties of the accretion shocks. Specifically, we assume that the baryonic mass follows the 1D EdS DM distribution, and that the temperature and metallicity are uniform inside the CGM. Nevertheless, as we will demonstrate in the following sections, it approximately (to within $\sim$half a dex) reproduces the observed column densities, both within and beyond $R_{\rm vir}$. Furthermore, being 1D, our models do not capture potential deviations from spherical symmetry, such as varying covering fractions, directional streams, etc. Our primary objective in this paper is to assess the contribution of the IGM to the warm-ion absorption, and we consider this simplified model to be adequate for this specific purpose.

3. Results

In this section, we present the results of our toy model for the O VI absorption lines arising in galactic halos and their surroundings. We discuss the ion fraction (Section 3.1) and integrated column densities (Section 3.2), examine the sensitivity to the assumed metallicity (Section 3.3), and explore the kinematic absorption-line profiles (Section 3.4). Later, in Section 4, we use these results to highlight the key takeaway of this paper—that IGM column densities may be comparable to observed values—by directly comparing our model's IGM-only predictions with the observations of K. Tchernyshyov et al. (2022).

3.1. Ion Fractions

Figure 1 shows the evolution of our fiducial halo model for a halo that attains a mass of $10^{12}\,M_\odot$ at a redshift $z = 0$, with $f_{\rm shock} = 1$ ($R_{\rm shock} \approx 215$ kpc at $z = 0$). The evolution of various quantities is shown using color maps on the redshift–radius plane. The bottom-left panel shows the evolution of the gas temperature. The gas temperature is determined either by equilibrium with the UV background radiation at the local density or by the shock temperature for virialized gas—if it is larger than the equilibrium temperature—following Equation (6). The baryonic gas density is shown in the top-left panel and follows from Equation (4).

We display the evolving ion fraction distributions for C III, C IV, O VI, and O VII in the middle and right columns of Figure 1. The ion fractions at CPIE are functions of temperature, density, and redshift. Note that while the density profile $\rho(r)$ varies slowly with redshift, the virial temperature and the intensity of the UV background radiation are stronger functions of z. Consequently, the ion fractions at a given density are also redshift dependent.

Figure 1 confirms that far from the halo the density approaches its undisturbed mean value, resulting in an equilibrium temperature of $T_{\rm PIE} \sim 5 \times 10^4$ K. Warm ions are produced in this dilute warm gas due to photoionization. As the IGM gas falls toward the halo, the gas density ($\rho_{\rm gas}$) rises while the equilibrium temperature ($T_{\rm PIE}$) drops, enhancing the

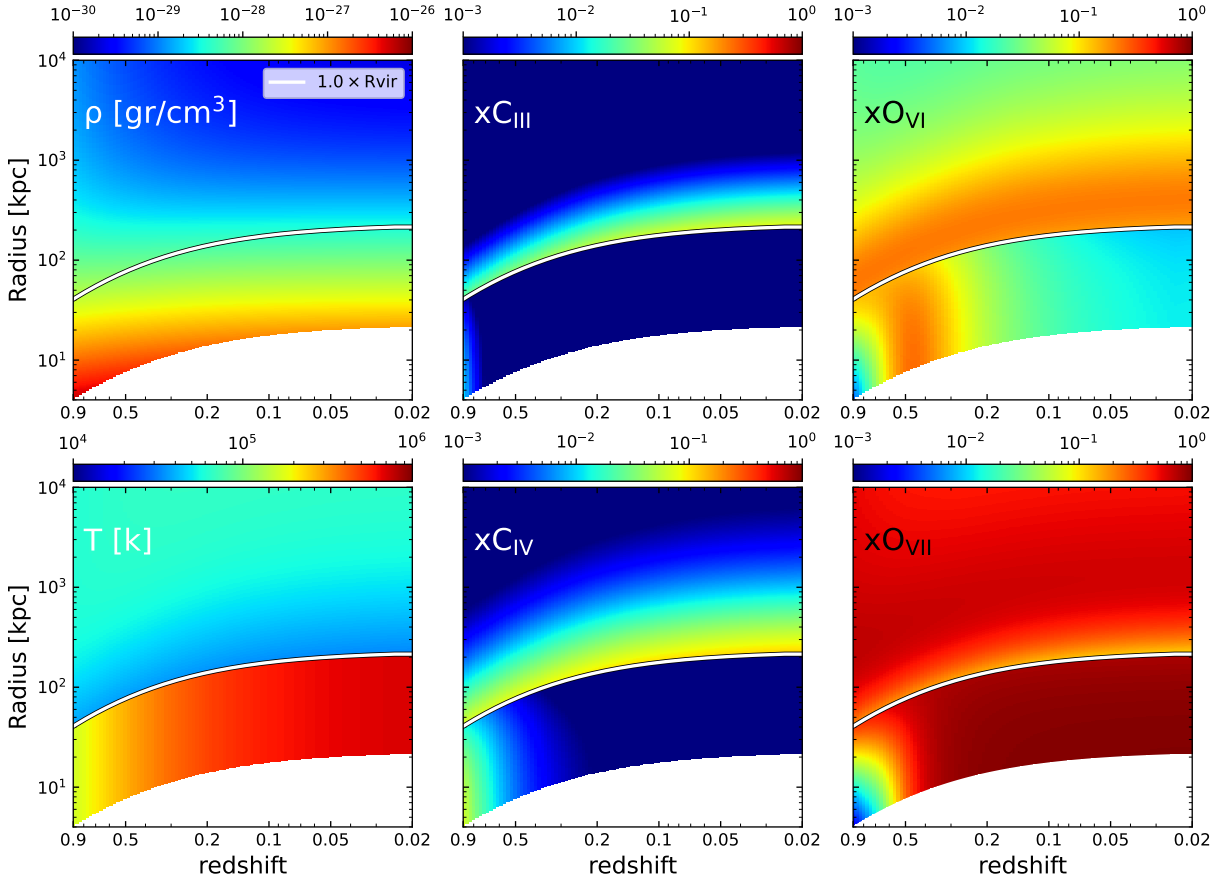

Figure 1. Radius–redshift diagrams for a $M_{z=0} = 10^{12}\,M_{\odot}$ halo, color-coded by different quantities. Top left: baryonic gas density. Bottom left: gas temperature. Top middle: C III ion fraction. Bottom middle: C IV ion fraction. Top right: O VI ion fraction. Bottom right: O VII ion fraction. The white curve in each panel shows the shock radius vs. redshift, with $f_{\rm shock} = 1$. We do not consider radii below $0.1R_{\rm vir}$.

production of warm ions such as C III, C IV, etc. The figure shows that significant fractions of warm ions are produced outside the virial radius, even at low redshifts. Specifically, O VI is efficiently produced in the low-density IGM down to $z = 0$. We also see that ions such as O VI can extend nearly a megaparsec beyond the CGM, forming a widespread envelope of ions around the halo.

Inside the CGM ($r < R_{\rm shock}$), collisional ionization at the virial temperature is generally the dominant ionization process. As the halo evolves it becomes more massive, and the CGM temperature increases from $\approx 10^5$ K at $z \sim 1$ to $\approx 10^6$ K at $z \approx 0$. Accordingly, the O VI ion fraction in our uniform CGM increases as the halo evolves, peaking at $z \sim 0.5$ before decreasing again. At $z \lesssim 0.5$, the CGM becomes hot enough to support the production of higher ions like O VII.

3.2. Column Densities

To test the detectability of the IGM component, we now compute the column densities at various impact parameters. As mentioned above, we define a CGM column as that arising from $r = 0.1R_{\rm vir}$ to $R_{\rm shock}$, and an IGM column as that arising from $r = R_{\rm shock}$ to 3 Mpc. The total column density is the sum of the two.

In Figure 2, we show our results for the total (solid) and IGM-only (dashed) O VI column densities versus the normalized impact parameter for halos at $z = 0.2$ and assuming $f_{\rm shock} = 1$ (see K. Tchernyshyov et al. 2022, Figure 4 therein). We emphasize that our simplified toy model is intended for an order-of-magnitude analysis of the IGM's potential contribution to warm-ion absorption, rather than for precisely reproducing the observed columns. The different panels in Figure 2 correspond to different halo mass bins, with the upper-left panel showing the lowest-mass bin ($7.8 < \log M_* < 8.5$) and the lower-right panel showing the highest-mass bin ($10.4 < \log M_* < 11.2$). Within each panel, we plot models for the two masses, roughly bracketing the displayed range, with orange curves for the high mass and blue curves for the low mass in that bin. We also display in the different panels of Figure 2 the observational CGM data set compiled by K. Tchernyshyov et al. (2022, gray symbols) for galaxies at redshifts $0 < z < 0.6$, with a median redshift of 0.25. For each panel, we include both the detections (solid circles) and upper limits (open triangles) which match the mass range of that bin.

Figure 2 shows that our highly simplified model produces O VI column densities comparable to observations. It also demonstrates that the IGM-only columns are comparable to observations, and that they are often also comparable to the total columns, except in the inner portions of halos with masses $9 \lesssim \log M_*/M_{\odot} \lesssim 10$. We thus argue that the near-halo IGM may significantly contribute to observed warm-ion column densities in CGM surveys. Furthermore, we note that although the decline of O VI column densities with impact parameter in our model is very shallow, it gradually decreases to values of $\lesssim 10^{13.5}\,{\rm cm}^{-2}$ at radii beyond a few times $R_{\rm vir}$. These values approach the typical sensitivity limits of many observational surveys and are consistent with the large number

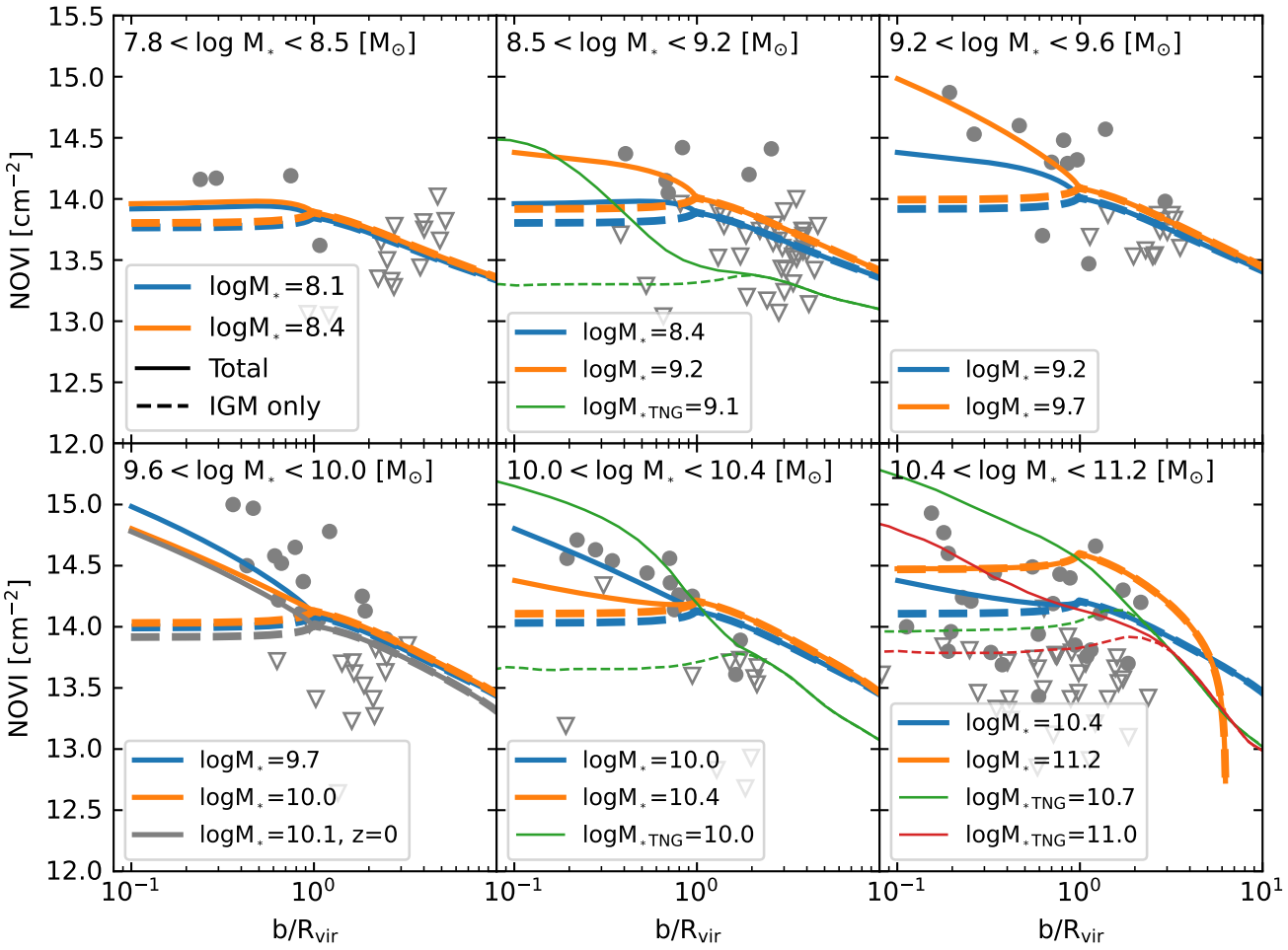

Figure 2. O VI columns vs. normalized impact parameter for $z = 0.2$, $f_{\rm shock} = 1$ halos. Each panel corresponds to a different mass bin (as labeled). In each panel, we display two models corresponding to the highest-mass (orange) and lowest-mass (blue) halos within that bin. For both models we show our total (solid) and IGM-only (dashed) O VI columns. The data points are the K. Tchernyshyov et al. (2022) compilation of CGM observations, including detections (solid circles) and upper limits (empty triangles). The green and red curves correspond to the median O VI columns from IllustrisTNG at $z = 0$ (D. Nelson et al. 2018), where available. The different redshift of the IllustrisTNG models has little effect, as is demonstrated by our gray $z = 0$ curve in the lower-left panel, which is very similar to the $z = 0.2$ orange curve.

of upper limits reported at these radii (e.g., K. Tchernyshyov et al. 2023; Z. Qu et al. 2024).

For comparison, we also display in Figure 2 the median O VI column densities computed by D. Nelson et al. (2018) from the IllustrisTNG simulations, when available. These are shown by the green and red curves, with masses indicated in the legends. In addition to the total column densities (solid curves), D. Nelson et al. (2018) also provide an "other" component, emanating from IGM gas and satellite halos (dashed curves).

Note that the D. Nelson et al. (2018) columns are for $z = 0$ halos, whereas our curves are for $z = 0.2$ halos to allow for a more direct comparison with observations. To estimate the impact of this difference in redshift, we plot in the bottom-left panel of Figure 2 our result for a $z = 0$, $M_* = 1.25 \times 10^{10}\,M_\odot$ halo. Comparing that with the orange $z = 0.2$ curve, we see that the differences are very small. We verified that the differences are minor in all other mass bins as well, but did not display the $z = 0$ curves to avoid clutter.

Figure 2 shows that our models generally produce a more gradual slope overall than D. Nelson et al.'s (2018), and that while our IGM columns are typically a factor ∼2–3 larger, we obtain a similar overall trend to the IllustrisTNG IGM curves. Nelson's more realistic 3D models indicate a higher CGM contribution to the total column in the central parts of massive halos. We also note, that due to the 3D nature of the IllustrisTNG data, the "total" and "other" components only converge at 2–3× $R_{\rm vir}$. The gross agreement of our computed columns with both observations and complex 3D simulations serves as a sanity check when using our simplified model to estimate IGM contributions to O VI column densities.

To explore how the overall IGM contribution fractions depend on halo mass, and to compare our results with other works, we now consider surface-averaged columns—representing the entire halo—as was previously done in D. Nelson et al. (2018) and K. Tchernyshyov et al. (2022).

To determine the surface averages, we first calculate the total and IGM columns as functions of the impact parameter, b.[7] Subsequently, we surface-average these columns over impact parameters ranging from $b = 0.1R_{\rm vir}$ to $b = R_{\rm vir}$, enabling a direct comparison with published results.

The top panel of Figure 3 shows the surface-averaged total (solid) and IGM-only (dashed) O VI column densities versus the halo's stellar mass, M_*. The corresponding halo masses are

[7] As before, integrating from max($0.1R_{\rm vir}$, b) to 3 Mpc for the total column and from $R_{\rm shock}$ to 3 Mpc for the IGM columns.

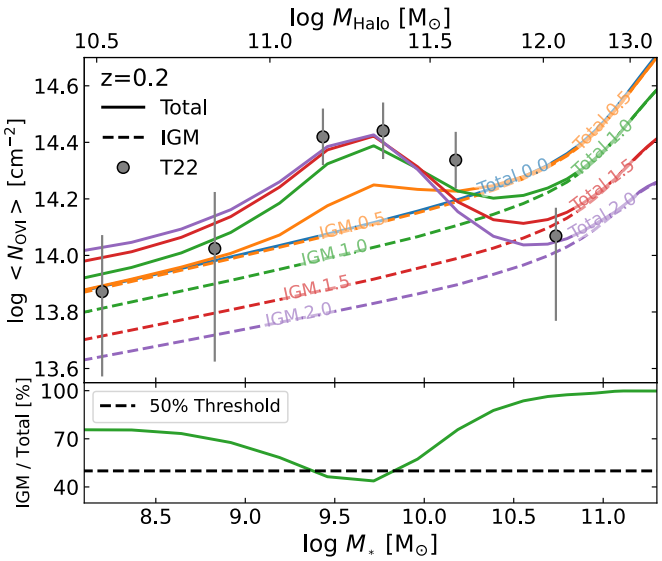

Figure 3. Top: surface-averaged values of O VI column densities (averaged within R_{vir}; see text) vs. stellar mass . The solid curves show the total column densities, and the dashed curves show the IGM column densities. Different colors are for different values of f_{shock} (see labels). The gray markers display the CGM^2 results from K. Tchernyshyov et al. (2022). Bottom: fraction (percent) of the IGM-only O VI column from the total O VI column densities for $f_{shock} = 1$. The dashed horizontal line marks a 50% IGM contribution to the total estimated columns.

shown on the top axis. The stellar masses were obtained using the stellar-to-halo mass relation presented in G. Girelli et al. (2020, Equation (6) and Table 1 therein). Different colors are for different values of f_{shock}. The gray symbols display the CGM^2 detections from K. Tchernyshyov et al. (2022). We find that our model captures the general trend revealed by the observations. For $f_{shock} = 1$, the toy model agrees with the observed value to better than 50%, even when the CGM dominates. We also display a "no-halo" curve (with $f_{shock} = 0$, in blue) to illustrate the contribution expected from halos which have yet to form a stable shock.

For halo masses $\lesssim 10^{12}\,M_\odot$, our highly simplified model exhibits a trend similar to the prediction made by Z. Qu & J. N. Bregman (2018b). It is also qualitatively similar to the IllustrisTNG results presented in D. Nelson et al. (2018), albeit shifted by approximately half a decade to lower masses (see Figure 6 in K. Tchernyshyov et al. 2022). Our model typically underpredicts the average observed column by 0.1–0.2 dex. This could be because our assumed CGM metallicities are too low, or because of the more complex thermal and dynamical structure of realistic halos.

For high-mass halos ($M_{vir} \gtrsim 10^{12}\,M_\odot$) in the group to cluster regime, the O VI column densities in our models increase monotonically with halo mass. This is a natural result of the increasing path length through the dense IGM: In the spherical collapse models, the density profiles are self-similar, with all radii scaling as $\propto M_{halo}^{1/3}$ (e.g., J. E. Gunn & J. R. Gott 1972). As a result, the IGM contribution—dominated by the denser regions just outside the halos—also scales accordingly. In contrast, observational data do not indicate a mass-dependent increase, with observed group columns spanning the range $13.5 \lesssim \log N_{O\,VI} \lesssim 14.9$ for halo masses $13.5 \lesssim \log M_{vir}/M_\odot \lesssim 14.5$ (e.g., J. T. Stocke et al. 2019). There are several possible explanations for why realistic group- and cluster-sized structures might fail to produce significant O VI columns, despite having thicker blankets of dense IGM. For instance, J. T. Stocke et al. (2019) suggest that CGM absorbers in group-sized halos do not possess sufficient relative radial velocities to escape from these groups, which could imply that metals remain confined within the virial radius, a notion also supported by hydrodynamical simulations (such as IllustrisTNG; e.g., D. Nelson et al. 2018). This could imply a mass-dependent IGM metallicity that decreases in larger structures. Alternatively, radiation from hotter accretion shocks may overionize the gas relative to the metagalactic background, or the gas may become collisionally ionized as it is shock-heated while accreting onto filaments and substructure in the dense cosmic web near more massive halos.

The nice agreement of our model with the CGM^2 data in the lower-mass range, $M_{vir} \lesssim 10^{11}\,M_\odot$, is particularly important: Low-mass galaxies are not expected to host stable CGMs due to the instability of their virial shocks (Y. Birnboim & A. Dekel 2003; A. Dekel & Y. Birnboim 2006). Therefore, any O VI observed around these galaxies likely originates from the IGM. This is further supported by the alignment of the $f_{shock} = 0$ and $f_{shock} = 0.5$ curves, which indicates the contribution from a small halo has little to no impact on the column densities. The agreement of our basic IGM model with observations in this mass range supports the idea that a simple, photoionized IGM plays a significant role in warm-ion absorption-line observations.

Finally, we note that the low-mass ($\lesssim 10^{11}\,M_\odot$) observations align most closely with the $f_{shock} = 0.5$ curve, while the high-mass ($\gtrsim 10^{12}\,M_\odot$) observations are nearest to the $f_{shock} = 2$ curve.[8] Although both the model and observational data have significant uncertainties, this pattern may suggest a trend of increasing shock-to-virial-radius ratio with halo mass. In addition, a halo-mass-dependent CGM metallicity could offer another avenue for improving the model's agreement to the observed average columns, particularly for halos with stellar masses of $\sim 10^{10}\,M_\odot$.

In the bottom panel of Figure 3, we display the fraction (percent) of the (halo-averaged) IGM column density from the (halo-averaged) total column density for $f_{shock} = 1$. The dashed horizontal line marks a 50% threshold. This figure indicates that, on average, the IGM contribution never drops below ~40% for our simplified CGM. Over a significant range of stellar masses, a significant O VI column—comparable to the observed values—seems to originate in the IGM. This suggests that physical processes associated with the IGM may play a larger role than often attributed when it comes to O VI absorption.

We now explore how these results depend on redshift, and whether they are specific to O VI or may apply to additional warm-ion absorption signatures. We thus repeat the analysis for halos with masses in the range 10^{11}–$10^{14}\,M_\odot$, at redshifts in the range $0.9 < z < 0.02$. In Figures 4 and 5, we display results assuming impact parameters $b = 100$ and 0 kpc, respectively. Since observations at $b = 0$ will realistically be dominated by the central galaxy, we only integrate starting at $0.1R_{vir}$, which we assume to be the galaxy radius. The columns for $b = 0$ represent the maximum possible CGM contribution. We display results for O VI, N V, and C IV.

Figure 4 follows the M_{vir}–z evolution of many halos. Each curve represents the evolution of a single halo and is color-coded by the fraction of IGM contribution to the total column density of O VI (left panel), N V (middle panel), and C IV (right

[8] In ΛCDM, halos are ~20% larger than in EdS cosmology. This can be characterized by $f_{shock} \simeq 1.2$, assuming the shock occurs at R_{vir}.

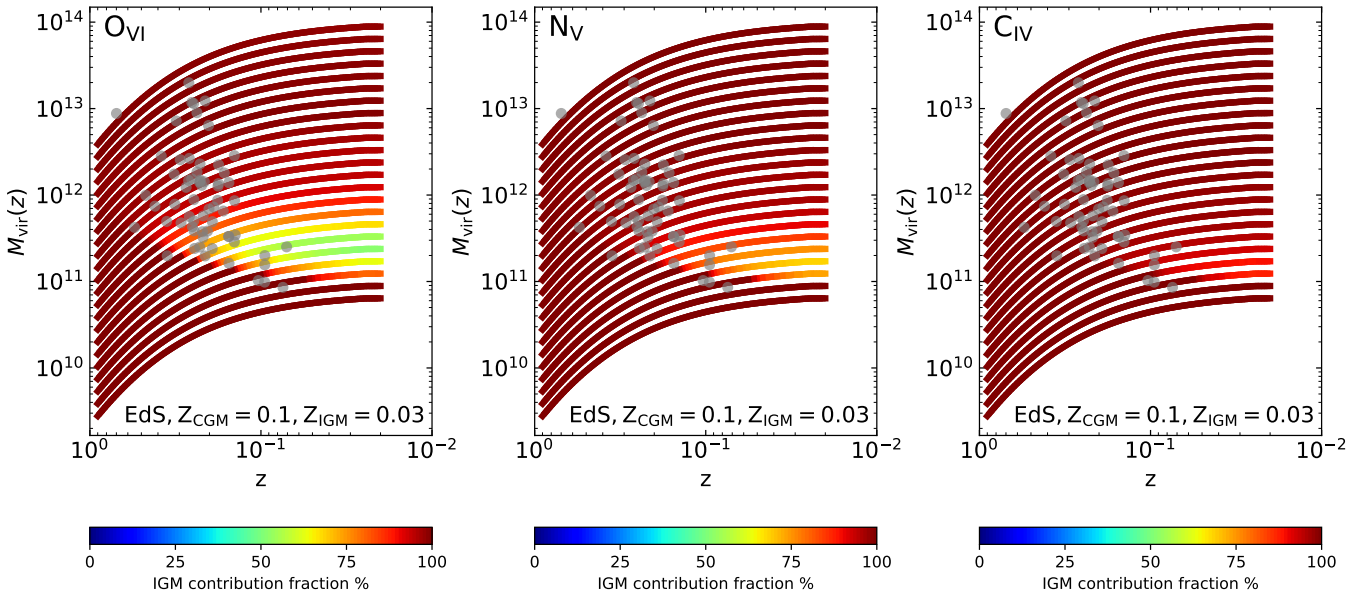

Figure 4. Virial mass vs. redshift curves, color-coded by the fraction of IGM contribution to the total columns at an impact parameter $b = 100$ kpc for our EdS $f_{shock} = 1$ halos, assuming the fiducial metallicity values $Z_{CGM} = 0.1\ Z_{\odot}$ and $Z_{IGM} = 0.03\ Z_{\odot}$. Each curve follows a single halo's trajectory. Left: O VI contribution fractions. Middle: N V contribution fractions. Right: C IV contribution fractions. The gray symbols indicate the position of the COS-Halos survey halos on this parameter space (J. K. Werk et al. 2016).

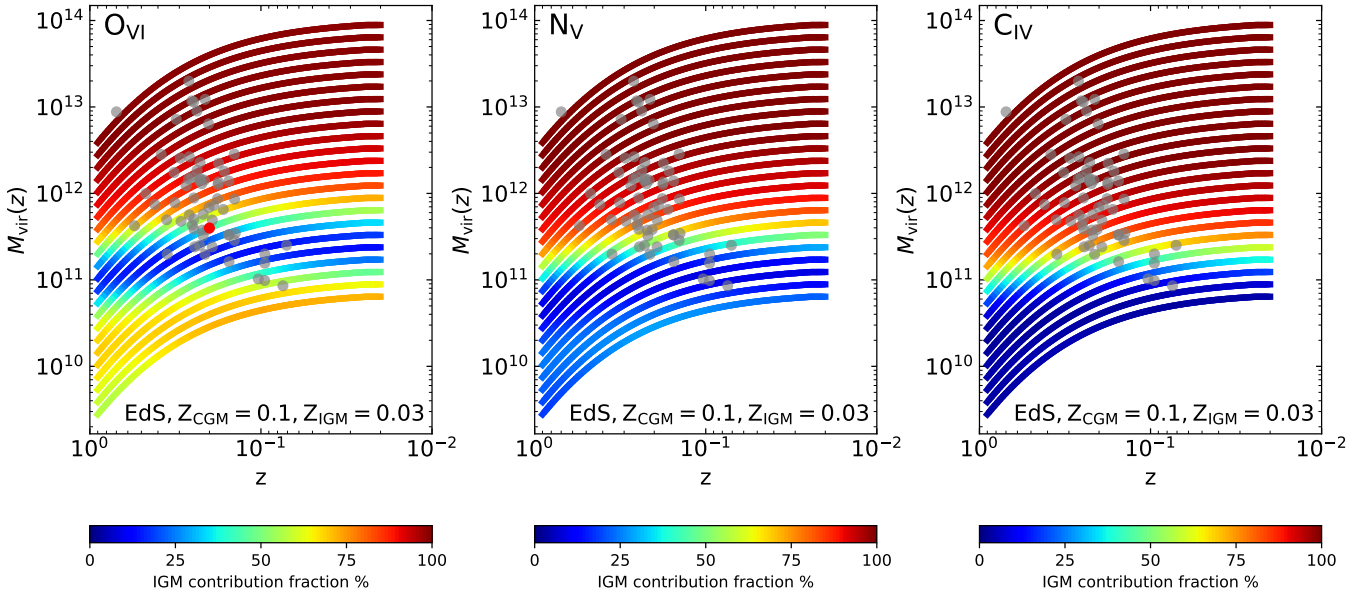

Figure 5. Same as Figure 4, but for an impact parameter $b = 0$ kpc. From left to right, we show the IGM contributions for the O VI, N V, and C IV column densities in our EdS $f_{shock} = 1$ halos, assuming the fiducial metallicity values $Z_{CGM} = 0.1\ Z_{\odot}$ and $Z_{IGM} = 0.03\ Z_{\odot}$. The gray symbols indicate the COS-Halos survey halos. The red marker in the left panel shows the parameters of the synthetic halo used in Section 3.3 for the metallicity-sensitivity exploratory tests.

panel). The fractions are evaluated at an impact parameter $b = 100$ kpc, assuming $f_{shock} = 1$. The figure shows that the IGM contribution is lowest for masses between 10^{11}–$10^{11.6}\ M_{\odot}$ and at low redshifts $z \lesssim 0.1$. Even then, the IGM contributes tens of percent of the total columns.

This trend may be readily explained by ion fraction distributions such as those displayed in Figure 1. At high redshifts (low halo masses), the virial temperature is too low and the halo gas density too high to allow efficient O VI production either via photoionization or via collisional ionization. Later, intermediate-mass halos have a virial temperature and densities ideal for efficiently producing O VI within the CGM, especially in the inner parts of the halo. As the halos further grow and evolve, the virial temperature surpasses the optimal CPIE value for O VI, thus diminishing the contribution of the CGM. The relative CGM contribution therefore has an optimal mass/redshift regime. The same logic follows for N V and C IV.

In the IGM, however, the ion fraction profiles weakly depend on halo mass or redshift, ensuring a steady contribution to the total observed columns. This is due to the concerted action of two effects: the decline in density with cosmic evolution, and the decreasing intensity of the UV background, which (for the redshift and mass range that we consider) result in a constant ionization parameter to within a factor of 2 in the nearby IGM.

Figure 4 shows that the IGM significantly contributes to the total column density. For reference, we also mark the position of the COS-Halos survey halos (J. K. Werk et al. 2013) on this parameter space. In all three panels, most observed halos reside well within the region where the IGM contribution to the absorption-line columns is expected to be significant. This gives further indication that interpreting the observed columns as emanating from the CGM exclusively may be inaccurate.

For completeness, we also show the IGM contribution fractions for lines of sight through the center of the halos (i.e., $b = 0$ kpc) in Figure 5. The lower impact parameter naturally maximizes the halo's contribution to the ion columns. This is both due to the larger path length through the halo and because the inner parts of the halo produce O VI more efficiently (see Figure 1). The corresponding IGM fractions are therefore lower. However, even in this case, the COS-Halos survey parameter space mostly resides in regions where the IGM contributes significantly to the observed columns.

3.3. Sensitivity to Metallicity Selection

In our models (see Section 2.3), we assume a uniform metallicity in all CGM halos ($0.1\,Z_\odot$) and throughout the IGM ($0.03\,Z_\odot$). In this section, we conduct exploratory calculations to illustrate the potential impact of the choice of metallicity on the observed columns.

First, we demonstrate the impact of changing the metallicity in a given model, both within the CGM and in the IGM beyond it. In Figure 6, we display the column density as a function of scaled impact parameter for a $4 \times 10^{11}\,M_\odot$ halo at $z = 0.2$. This halo falls well within the mass and redshift parameter space of the COS-Halos survey sample (see the red marker among the gray COS-Halos ones in Figure 5). The blue curve shows our fiducial parameters, in which the CGM metallicity is $0.1\,Z_\odot$ and the IGM metallicity is $0.03\,Z_\odot$. As in previous plots, the solid curves show the total O VI column, while the dashed curves display only the IGM contribution. The data points are the O VI column densities reported in K. Tchernyshyov et al. (2022) for stellar masses in the range $10.0 \leqslant \log M_* \leqslant 10.4$, encompassing the displayed ($\log M_* \simeq 10.2$) model halo. Note that this is a specific model for a particular mass and redshift, and therefore cannot be used to infer general conclusions about metallicity choices for the entire mass- and redshift-dependent population (e.g., Figure 2 shows that, for the fiducial metallicity values, the $\log M_* = 10.0$ model better matches the CGM data points). Rather, it is intended only to demonstrate the impact of metallicity variations.

The orange and green curves show the O VI column in higher-metallicity halos: the orange curve shows a CGM metallicity of $0.2\,Z_\odot$, and the green curve is for $0.5\,Z_\odot$. As expected, halos with higher metallicities exhibit larger O VI column densities within $R_{\rm vir}$ due to the direct scaling of CGM O VI densities with Z within the virial heated halo. Note that the blue, green, and yellow curves overlap at $r/R_{\rm vir} > 1$.

The red and purple curves demonstrate the impact of increasing the IGM metallicity too: the red curves are for $Z_{\rm CGM} = 0.2\,Z_\odot$ and $Z_{\rm IGM} = 0.1\,Z_\odot$, and the purple are for $Z_{\rm CGM} = 0.5\,Z_\odot$ and $Z_{\rm IGM} = 0.2\,Z_\odot$. Because the IGM is heated and photoionized by the metagalactic background, its ion fractions depend on both density and metallicity. The metallicity dependence arises because the thermal equilibrium temperature is influenced by the metal abundance, which affects the cooling rates. The recombination rates and

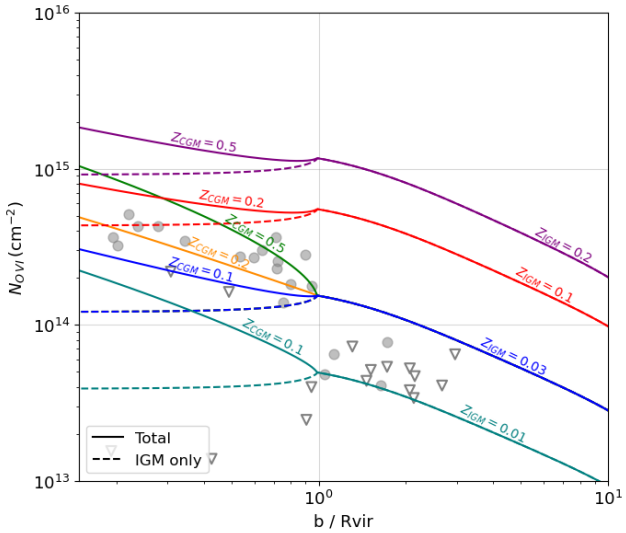

Figure 6. O VI column density vs. scaled impact parameter for various values of CGM and IGM metallicities (see legends) in a $4 \times 10^{11}\,M_\odot$ halo ($\log M_* = 10.2$) at $z = 0.2$. Solid curves are the total columns, and dashed curves show the IGM-only component. Our fiducial model is displayed in blue. In the orange and green curves we change only the CGM metallicity. In the red and purple curves we increase the IGM metallicity too. The cyan curve demonstrate the effect of decreasing the IGM metallicity. The symbols show O VI detections and upper limits for $10.0 \leqslant \log M_* \leqslant 10.4$ halos from K. Tchernyshyov et al. (2022).

associated ion fractions change accordingly. Therefore, the dependence of the column density on metallicity in the IGM is not necessarily strictly linear. Figure 6 shows, however, that the scaling is nearly linear with Z in the IGM too. We note, that in addition to the trivial change in O VI columns at $b > R_{\rm vir}$, changing the IGM metallicities also affects the O VI absorption well inside the halo (compare the red and orange, or the green and purple solid curves, which share the same CGM metallicity and differ only in IGM metallicity). Finally, in the cyan curve, we demonstrate the impact of lowering the IGM metallicity to $0.01\,Z_\odot$. A low-Z IGM significantly reduces the O VI columns beyond $R_{\rm vir}$, but also potentially at impact parameters within $R_{\rm vir}$. Low IGM metallicities may be more applicable to higher-mass galaxies that retain most of their produced metals inside the halos.

Next, we explore metallicities motivated by the halo's star formation history and metal yields, following M. S. Peeples et al. (2014). For our $z = 0.2$, $M = 4 \times 10^{11}\,M_\odot$ halo, the stellar mass is $\sim 1.5 \times 10^{10}\,M_\odot$, yielding $\sim 8 \times 10^8\,M_\odot$ in metals, of which ~40% are expected to be in O VI-bearing CGM gas (M. S. Peeples et al. 2014). For our $f_{\rm shock} = 1$ fiducial halo, this implies a CGM metallicity of 1.3 times solar.

We then consider different values of $f_{\rm shock}$, but this time retaining the same metal mass within the shocked region, so that the metallicity is higher for lower $f_{\rm shock}$ and vice versa. Figure 7 presents the O VI column densities that arise in halos with $f_{\rm shock} = 0.5, 0.66, 1, 1.5$, and 2. The K. Tchernyshyov et al. (2022) detections and limits for $10.0 \leqslant \log M_* \leqslant 10.4$ halos are again shown by the symbols. As before, the specific displayed model is intended solely to illustrate the impact of metallicity variations, rather than to draw general conclusions about metallicity values for the entire population.

Because of the increased metallicities inside smaller halos, the O VI columns at small impact parameters are much larger, but they drop to the "background" values at lower physical

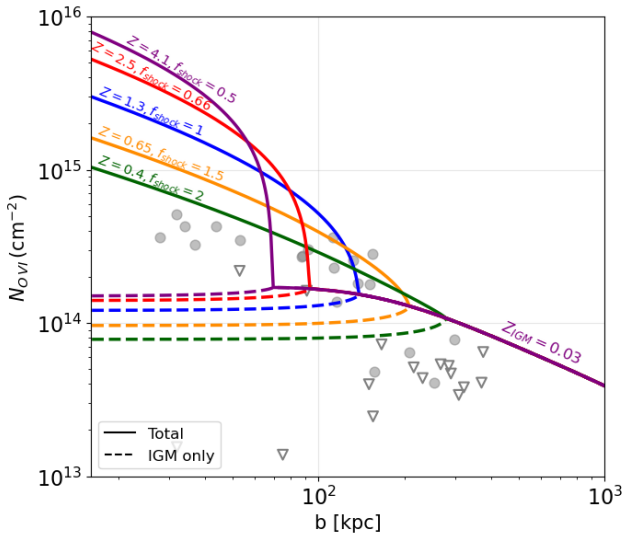

Figure 7. O VI column density vs. impact parameter for various values of $f_{\rm shock}$ in a $4 \times 10^{11}\,M_{\odot}$ halo at $z = 0.2$. The total CGM O VI-bearing gas mass is kept constant across the different $f_{\rm shock}$ values, so that the metallicity is higher in smaller halos (see legends near curves). As before, solid curves are the total columns and dashed curves show the IGM-only component. The symbols show O VI detections and limits for the $10.0 \leqslant \log M_{*} \leqslant 10.4$ halos from K. Tchernyshyov et al. (2022).

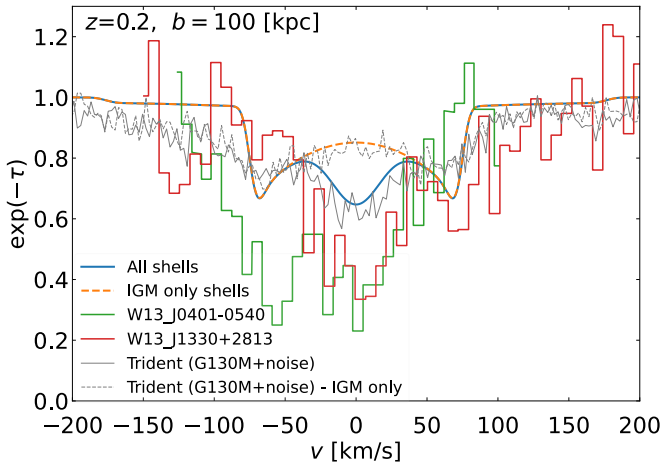

Figure 8. Simulated absorption-line profiles for a $10^{12}\,M_{\odot}$ halo at $z = 0.2$ assuming an impact parameter $b = 100$ kpc. The blue curve is the profile including all gas between $0.1R_{\rm vir}$ and 3 Mpc. The dashed orange curve is for IGM only (namely, $R_{\rm shock}$–3 Mpc). The solid gray curve is a synthesized absorption-line profile created with the Trident Python package, which includes Milky Way foreground, line-spread function, and Gaussian noise. The dashed gray curve is the Trident result for the IGM only.

impact parameters.[9] Compared to those, larger halos (i.e., larger $f_{\rm shock}$) produce smaller columns inside the halos, but the elevated CGM contributions extend to larger impact parameters.

3.4. Simulated Absorption-line Profiles

Our simple 1D models suggest that significant fractions of O VI and other warm ions observed in CGM surveys may arise in the photoionized IGM surrounding the shocked halos. We therefore explore whether the two components may be kinetically distinct. For this purpose, we compute the line profiles that are expected to arise due to the combined contributions of the virialized hot CGM and the warm, photoionized infalling IGM. As described in Section 2.5, we assume thermal broadening within each shell, as we integrate through the line-of-sight velocity profile for a given impact parameter (see the Appendix). We verify our procedure by comparing to mock observations of COS synthesized from our profiles by the Trident numerical package, as well as to observed line profiles from J. K. Werk et al. (2013).

Figure 8 shows a comparison between our results for the absorption-line profile of the total gas (solid blue), and that of the IGM only (dashed orange). It also shows the absorption-line profiles produced by the Trident Python package for the same data for the total gas (solid gray) and the IGM-only (dashed gray). The Trident profiles also include Galactic foregrounds and noise to mimic HST-COS observations.

There is an apparent difference between the total and the IGM-only profiles near the line center, where the hot, virialized, low-velocity CGM gas is present. Aside from the line center, there are two absorption "dips," one from each side of the center. These are a result of the infalling IGM gas, as well as the expanding gas beyond the turnaround radius. The infall velocity is largest at $R_{\rm shock}$, where the gas is closest to the halo. This is also where the IGM density is maximal. The maximal infall velocity is set by the ratio between the halo mass and its radius ($v_{\rm max}^2 \approx GM_{\rm vir}/R_{\rm shock}$). A well-resolved kinematic structure of an absorption line may thus allow us to discern IGM from CGM contributions, as well as constrain the halo's physical characteristics. For example, a kinematic structure composed of only two distinct absorption components may indicate that the IGM contribution dominates over the CGM columns.

Our 1D toy-model kinematic profiles are naturally simplistic, but they exhibit similarities with several properties identified in broad O VI absorption observations (J. K. Werk et al. 2016). First, our broad CGM+IGM O VI absorption profiles, even when the IGM contributes significantly, are generally centered and weighted near the halo's velocity centroid. This will naturally explain the kinematic alignment with lower ions. Second, the O VI absorption naturally combines collisionally ionized gas from the CGM and photoionized gas from the IGM, consistent with findings that O VI is unlikely to originate from a single ionization mechanism (J. K. Werk et al. 2016). Although these qualitative trends align well with observations, the detailed distributions and physical properties in the observational data require more sophisticated and physically complex models for meaningful comparison.

While the kinematic difference between the total and IGM-only profiles seems sufficient for differentiation in our toy model, this "three-dip" structure will likely often not be distinct in observations of astrophysical halos due to the complex morphology and kinematics of their multiphase CGM.

To compare our idealized profiles with observational data, we display as examples in Figure 8 data for two absorption-line profiles extracted from J. K. Werk et al. (2013), for J1330 +2813 (red) and J0401-0540 (green). Both lines exhibit stronger overall absorption than in our model, which may be attributed to higher metallicity in the CGM (for the central

[9] This may suggest that the overall metal yield or the fraction of mass in the CGM O VI-bearing gas in M. S. Peeples et al. (2014) is overestimated, but more realistic CGM models are needed to test this possibility.

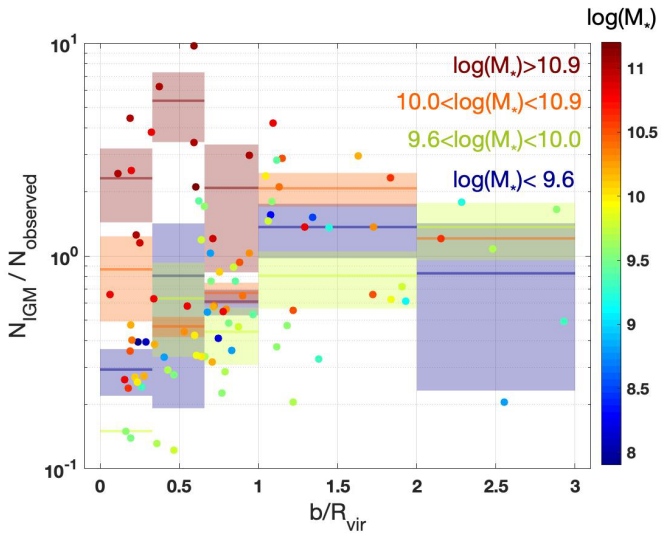

Figure 9. Fraction of the observed O VI columns that can be attributed to the IGM. For each detection in the K. Tchernyshyov et al. (2022) data set, we plot the ratio between our model's IGM-only O VI column—evaluated at the observed redshift, stellar mass, and impact parameter—and the observed column as a function of the scaled impact parameter ($b/R_{\rm vir}$). The symbol colors indicate stellar mass, as shown by the color bar on the right. We also display the average ratios (horizontal bars) and their associated errors (shaded regions), divided into four stellar mass bins. The colors and labels in the plot indicate the corresponding mass bins. The horizontal extent of the bars represents our impact parameter bins.

dips) or in the IGM (for the side dips). The J1330+2813 line shows a dip structure similar to the one in our model, consisting of one central dip (at $v \simeq 0\,{\rm km\,s^{-1}}$), and two additional dips, one on each side of the line center ($v \simeq -130, 75\,{\rm km\,s^{-1}}$). The J0401−0540 line shows a different structure, with two prominent dips ($v \simeq 0,\ -50\,{\rm km\,s^{-1}}$). Such structures may hint at additional contributions to the profile other than the static halo, such as outflows, satellites, asymmetric accretion, etc.

4. Conclusions

The main results of our analysis are presented in a complementary way in Figure 9. This figure directly compares the column densities produced in the photoionized IGM with observations, avoiding any uncertainties introduced by our crude CGM model. In doing so, it highlights the key takeaway of our work.

The symbols display the ratio between our IGM-only O VI columns and the observed values from K. Tchernyshyov et al. (2022) as a function of the scaled impact parameter, $b/R_{\rm vir}$. The symbols are color-coded by stellar mass, ranging from blue (low masses) to red (high masses). For each observed data point, we compute a corresponding model at the observed redshift and stellar mass. The model's IGM-only O VI column density is then extracted at the observed impact parameter, and is used to compute the ratio displayed in Figure 9. The figure reveals a large scatter in the IGM-to-observed ratio inside the halo ($b/R_{\rm vir} < 1$), which diminishes outside the halo—converging to values of order unity.

We divide the data into four mass bins, as indicated by the legend and color. For each bin, we compute the mean ratio of the model's IGM-only O VI column to the observed column ($N_{\rm IGM}/N_{\rm obs}$) across several impact parameter ranges. These mean ratios are displayed by the horizontal bars in Figure 9, with their extent indicating the impact parameter bins. The shaded regions surrounding the bars show the standard error on the mean values.

Figure 9 confirms that for the most massive halos our IGM model tends to overproduce the O VI columns inside $R_{\rm vir}$ (see the bottom-right panel of Figure 2, rightmost point in Figure 3, and the discussion of this discrepancy in Section 3.2). Since no observations exist for such massive halos beyond $R_{\rm vir}$, no mean ratio is displayed for $b > R_{\rm vir}$.

For halo masses below $\sim 10^{12}\,M_\odot$, Figure 9 indicates that the IGM column densities constitute (on average) tens of percent of the total observed column inside $R_{\rm vir}$ and approach values of order unity outside $R_{\rm vir}$ (as they should). Only detections are included in Figure 9, as more realistic 3D models are needed to assess the possibility of nonunity covering fractions for the warm gas.

This plot affirms our conclusion that the IGM may produce significant amounts of O VI, comparable to observed values, across masses and impact parameters. By directly comparing only the IGM component of the model with observations, we avoid uncertainties introduced by our oversimplified CGM model.

5. Summary and Discussion

In this work, we used a simple 1D toy model to compute the cosmological collapse of DM halos and their baryonic content around small initial density perturbations. We computed the distributions and densities of the DM and gas as functions of time, from redshift $z = 100$ up to the present day assuming a spherical collapse of the DM in an expanding EdS universe. We estimate the virial temperature inside the halo following J. L. Johnson (2012). In our fiducial models, we assume uniform metallicities of $Z_{\rm CGM} = 0.1\ Z_\odot$ within the halo and $Z_{\rm IGM} = 0.03\ Z_\odot$ in the IGM. Using CLOUDY, we obtained the gas PIE temperatures due to the UV background radiation, and the ion fractions of various ions both outside (PIE) and inside (forcing the temperature to $T_{\rm vir}$ when $T_{\rm vir} > T_{\rm PIE}$) the evolving halo.

Our results indicate that a significant fraction of the column densities of warm ions (O VI, N V, and C IV) observed near galaxies may originate from the inner IGM envelopes of the shocked CGM. The IGM envelopes are often neglected when interpreting such observations.

We compute the IGM contribution to the production of warm ions as a function of the virial mass and redshift. We show that the IGM warm-ion columns depend on the halo's virial mass and on the impact parameter. For example, the minimum IGM contribution for O VI columns is obtained for $M \simeq 10^{11}$–$10^{11.6}\,M_\odot$. Even then, the IGM contribution remains significant and comparable to observed values.

For the mass range probed by most CGM surveys (which is typically $\gtrsim 10^{11.5}\ M_\odot$), our model indicates that the IGM contribution to the total columns is significant.

The mass-dependent column densities computed with our models are in qualitative agreement with observational data, both within and outside the halos (see Figure 2). They also roughly match the surface-averaged values (Figure 3).

Our CGM model is quite basic, and therefore fails to capture numerous intricate aspects of astrophysical halos, such as the morphological, thermal, and dynamical details of the multiphase CGM, or the radiative and dynamical properties of accretion shocks. As a result, it is not a suitable model to

quantitatively compute the CGM columns. Moreover, the column densities predicted by our model are sensitive to the assumed density and metallicity profiles. However, our focus in this work has not been on quantitatively reproducing the observed column densities, but rather on qualitatively assessing the IGM's contribution to the warm-ion absorption. We find our simplified model to be adequate for this specific purpose.

Despite its limitations, our model qualitatively (to within ∼half a dex) matches the observed column densities both inside and outside the halo for most halo–impact parameter combinations, and also agrees with more complex estimates based on 3D hydrodynamical simulation (see Figure 2). Furthermore, a direct comparison of our IGM-only columns with observations—avoiding uncertainties introduced by a crude CGM model—suggests that the IGM typically contributes tens of percent of the observed columns inside $R_{\rm vir}$ (see Figure 9).

Finally, we composed synthetic absorption-line profiles to test whether the CGM and IGM contributions to the total absorption may be discerned kinematically. We demonstrated that a typical line profile is composed of a central (zero-velocity) wide component arising due to the hot CGM, and of two velocity-shifted features that emanate from the infalling IGM envelopes and expanding gas beyond the turnaround radius, forming a "three-dip" structure. These synthetic spectra should, however, be taken with a grain of salt, since real-life halos do not have a perfectly static (zero-velocity) CGM, but rather exhibit complex velocity structures; galactic winds, stellar activity, and turbulence may all contribute to velocities of order hundreds of kilometers per second anywhere up to the virial radius. Thus, separating the CGM and IGM contributions in observed profiles will likely prove challenging (see Figure 6). Additional complications may arise due to asymmetric infall of the IGM, with filaments, sheets, and satellites affecting line profiles, as often observed.

We conclude that the photoionized IGM envelopes of galactic halos may contribute significantly to the observed warm-ion column densities in CGM surveys. This contribution should be taken into account when attempting to gain insight into the physical processes in the CGM. The inclusion of an IGM contribution may affect the inferred thermal properties and the conclusions regarding the role of nonthermal components and instabilities inside halos.

In a follow-up work, we intend to extend this study to include a more realistic, hydrodynamic ΛCDM halo collapse model which better represents the formation and structure of virial shocks. We will also include the influence of the UV background and local ionizing sources, and take departures from ionization equilibrium into account. Our more realistic model may be more directly applicable to interpreting CGM observations.

Acknowledgments

We thank the anonymous referee for the constructive and thoughtful review, which provided valuable suggestions and helped us improve our paper. This research was supported by the Israel Science Foundation (grant No. 2190/20).

Software: Astropy (Astropy Collaboration et al. 2013, 2018, 2022), CLOUDY (G. J. Ferland et al. 2017; M. Chatzikos et al. 2023), YT analysis toolkit (M. J. Turk et al. 2011) TRIDENT (C. B. Hummels et al. 2017).

Appendix
Kinematic O VI Absorption Spectrum

In Section 3.4, we present synthetic O VI absorption spectra for lines of sight passing through our computational box. Given an impact parameter b, the line of sight passes through all the shells with radial distances between b and 3 Mpc.

Each shell is characterized by its distance from the halo center r_i, O VI number density $n(\mathrm{O\,VI})_i$, temperature T_i, and velocity relative to the halo centroid v_i. The projected line-of-sight velocity of a shell is then $v_{i,\parallel} = v_i\sqrt{1-(b/r_i)^2}$ (note, $b < r_i < 3$ Mpc). When computing the total absorption through the halo, each shell contributes twice—on the near and far sides of the halo—with opposite line-of-sight velocities, i.e., at $\pm v_{i,\parallel}$.

For the temperatures and optical depths characteristic of the CGM and IGM, the individual shell's line profiles are dominated by thermal broadening, and can therefore be well approximated by Gaussian profiles (e.g., Equation (6.38) from B. T. Draine 2011, expressed in terms of velocity):

$$\phi_i^{\pm}(v) \approx \frac{1}{\sqrt{\pi}\,b_i}\exp\left(-\frac{(v \pm v_{i,\parallel})^2}{b_i^2}\right),$$

which are centered about $\pm v_{i,\parallel}$ for the near and far sides of the halo. Here, $b_i = \sqrt{2k_BT_i/m}$ are the Doppler-broadening parameters, and $\int\phi_i^{\pm}(v)dv = 1$. For O VI absorption, we set $m = m_{\rm O} \simeq 16m_p$. With this line profile, the absorption cross section is given by (e.g., B. T. Draine 2011, Equation (6.39) therein)

$$\sigma_i^{\pm}(v) = \frac{\pi e^2}{m_e c} f\ \lambda_0\ \phi_i^{\pm}(v) = \frac{\sqrt{\pi}\,e^2}{m_e c}\ \frac{f\lambda_0}{b_i}\ e^{-(v\pm v_{i,\parallel})^2/b_i^2},$$

where f is the oscillator strength for the transition. For our O VI line at $\lambda_0 = 1031.91$ Å, the oscillator strength is $f(\mathrm{O\,VI}) = 0.1376$.[10]

The optical depth is then

$$\tau_v = \sum_i [\sigma_i^+(v) + \sigma_i^-(v)]\,n(\mathrm{O\,VI})_i\,ds_i,$$

where ds_i is the path length through shell i along the line of sight, $ds_i = (r_{i+1} - r_i)/\sqrt{1-(b/r_i)^2}$.

Finally, the velocity-dependent intensity is given by

$$I(v) = I_0(v)e^{-\tau_v}.$$

In creating Figure 6, we assumed a flat incoming spectrum $I_0(v)$.

ORCID iDs

Itai Bromberg https://orcid.org/0000-0002-9495-8767
Kartick C. Sarkar https://orcid.org/0000-0002-7767-8472
Orly Gnat https://orcid.org/0000-0002-4244-0237
Yuval Birnboim https://orcid.org/0000-0002-6547-8545

References

Appleby, S., Dave, R., Sorini, D., Cui, W., & Christiansen, J. 2023, MNRAS, 519, 5514
Astropy Collaboration, Price-Whelan, A. M., Lim, P. L., et al. 2022, ApJ, 935, 167

[10] www.atomdb.org

Astropy Collaboration, Price-Whelan, A. M., Sipőcz, B. M., et al. 2018, AJ, 156, 123
Astropy Collaboration, Robitaille, T. P., Tollerud, E. J., et al. 2013, A&A, 558, A33
Birnboim, Y., & Dekel, A. 2003, MNRAS, 345, 349
Chatzikos, M., Bianchi, S., Camilloni, F., et al. 2023, RMxAA, 59, 327
Dalton, T., Morris, S. L., Fumagalli, M., & Gatuzz, E. 2021, MNRAS, 508, 1701
Dalton, T., Morris, S. L., Fumagalli, M., & Gatuzz, E. 2022, MNRAS, 513, 822
Dekel, A. 1981, A&A, 101, 79
Dekel, A., & Birnboim, Y. 2006, MNRAS, 368, 2
Draine, B. T. 2011, Physics of the Interstellar and Intergalactic Medium (Princeton, NJ: Princeton Univ. Press)
Faerman, Y., Sternberg, A., & McKee, C. F. 2017, ApJ, 835, 52
Faerman, Y., Sternberg, A., & McKee, C. F. 2020, ApJ, 893, 82
Ferland, G. J., Chatzikos, M., Guzmán, F., et al. 2017, RMxAA, 53, 385
Gatuzz, E., Wilms, J., Hämmerich, S., & Arcodia, R. 2024, A&A, 683, A213
Girelli, G., Pozzetti, L., Bolzonella, M., et al. 2020, A&A, 634, A135
Gunn, J. E., & Gott, J. R., III 1972, ApJ, 176, 1
Gutcke, T. A., Stinson, G. S., Macciò, A. V., Wang, L., & Dutton, A. A. 2017, MNRAS, 464, 2796
Haardt, F., & Madau, P. 2012, ApJ, 746, 125
Ho, S. H., Martin, C. L., & Schaye, J. 2021, ApJ, 923, 137
Hummels, C. B., Smith, B. D., & Silvia, D. W. 2017, ApJ, 847, 59
Johnson, J. L. 2012, Formation of the First Galaxies: Theory and Simulations, Vol. 396 (Berlin: Springer), 177
Johnson, S. D., Chen, H.-W., & Mulchaey, J. S. 2015, MNRAS, 449, 3263
Lehner, N., O'Meara, J. M., Fox, A. J., et al. 2014, ApJ, 788, 119
Lehner, N., Wotta, C. B., Howk, J. C., et al. 2019, ApJ, 887, 5
McQuinn, M., & Werk, J. K. 2018, ApJ, 852, 33
Muzahid, S., Srianand, R., Bergeron, J., & Petitjean, P. 2012, MNRAS, 421, 446
Nelson, D., Kauffmann, G., Pillepich, A., et al. 2018, MNRAS, 477, 450
Oppenheimer, B. D., Crain, R. A., Schaye, J., et al. 2016, MNRAS, 460, 2157
Oppenheimer, B. D., Schaye, J., Crain, R. A., Werk, J. K., & Richings, A. J. 2018, MNRAS, 481, 835
Peeples, M. S., Werk, J. K., Tumlinson, J., et al. 2014, ApJ, 786, 54
Planck Collaboration, Ade, P. A. R., Aghanim, N., et al. 2016, A&A, 594, A13
Prochaska, J. X., Weiner, B., Chen, H. W., Cooksey, K. L., & Mulchaey, J. S. 2011a, ApJS, 193, 28
Prochaska, J. X., Weiner, B., Chen, H. W., Mulchaey, J., & Cooksey, K. 2011b, ApJ, 740, 91
Qu, Z., & Bregman, J. N. 2018a, ApJ, 856, 5
Qu, Z., & Bregman, J. N. 2018b, ApJ, 862, 23
Qu, Z., Chen, H.-W., Johnson, S. D., et al. 2024, ApJ, 968, 8
Ryden, B. 2016, Introduction to Cosmology (2nd ed.; Cambridge: Cambridge Univ. Press)
Shen, S., Madau, P., Aguirre, A., et al. 2012, ApJ, 760, 50
Stern, J., Faucher-Giguère, C.-A., Hennawi, J. F., et al. 2018, ApJ, 865, 91
Stern, J., Hennawi, J. F., Prochaska, J. X., & Werk, J. K. 2016, ApJ, 830, 87
Stocke, J. T., Keeney, B. A., Danforth, C. W., et al. 2019, ApJS, 240, 15
Strawn, C., Roca-Fàbrega, S., Primack, J. R., et al. 2024, ApJ, 962, 29
Suresh, J., Rubin, K. H. R., Kannan, R., et al. 2017, MNRAS, 465, 2966
Tchernyshyov, K., Werk, J. K., Wilde, M. C., et al. 2022, ApJ, 927, 147
Tchernyshyov, K., Werk, J. K., Wilde, M. C., et al. 2023, ApJ, 949, 41
Tumlinson, J., Peeples, M. S., & Werk, J. K. 2017, ARA&A, 55, 389
Tumlinson, J., Thom, C., Werk, J. K., et al. 2011, Sci, 334, 948
Turk, M. J., Smith, B. D., Oishi, J. S., et al. 2011, ApJS, 192, 9
Voit, G. M. 2019, ApJ, 880, 139
Werk, J. K., Prochaska, J. X., Thom, C., et al. 2013, ApJS, 204, 17
Werk, J. K., Prochaska, J. X., Cantalupo, S., et al. 2016, ApJ, 833, 54
Wiersma, R. P. C., Schaye, J., & Theuns, T. 2011, MNRAS, 415, 353